frontiers | Frontiers in Materials

TYPE Original Research
PUBLISHED 24 August 2023
DOI 10.3389/fmats.2023.1264307

OPEN ACCESS

EDITED BY
Muhan Wang,
Qingdao University of Technology, China

REVIEWED BY
Weichao Guo,
Yanshan University, China
Junfeng Wang,
Liaoning University, China

*CORRESPONDENCE
Zhengxiang Liu,
lzxengineer@126.com

RECEIVED 20 July 2023
ACCEPTED 14 August 2023
PUBLISHED 24 August 2023

CITATION
Li Z, Liu Z, Zhang H, Luo Q and Long W-J (2023), Insights on the performance of sintered silt ash-blended cement: experiments and thermodynamic simulation.
Front. Mater. 10:1264307.
doi: 10.3389/fmats.2023.1264307

Insights on the performance of sintered silt ash-blended cement: experiments and thermodynamic simulation

Zhipeng Li[1], Zhengxiang Liu[2]*, Hongguang Zhang[3], Qiling Luo[4] and Wu-Jian Long[4]

[1]Key Laboratory of Earthquake Engineering Simulation and Seismic Resilience of China Earthquake, Tianjin University, Tianjin, China, [2]Poly Changda Engineering Co., Ltd., Guangzhou, China, [3]State Key Laboratory of Hydraulic Engineering Simulation and Safety, Tianjin University, Tianjin, China, [4]Guangdong Province Key Laboratory of Durability for Marine Civil Engineering, Shenzhen University, Shenzhen, China

The dredged silt exposed to the air is highly expected to be used to replace cement in large quantities due to its richness in aluminosilicates, which is in line with the dual-carbon background. Herein, a systematic exploration on the basic properties and hydration products of sintered silt ash-blended (SSA-blended) cement is conducted, using experiments and thermodynamic simulations. The results show that in the process of adding SSA to 50%, the compressive property and chloride ion permeation resistance are enhanced first and then weakened, whereas the flexural property is weakened gradually. Among them, with the addition of 10% SSA, the compressive strength can reach 65.2 MPa and the electric flux is 37.3% lower than that of Portland cement (PC), and the chloride ion permeability is rated as the lowest. As SSA increases, the FTIR spectra show that the reduction rates of bound water, ettringite and $Ca(OH)_2$ are accelerated gradually; SEM observation shows that the cement-based gelling skeleton has undergone a transition from dense to loose; the thermodynamic simulation results show that C-S-H increases first and then decreases, implying that SSA has a certain pozzolanic activity. In addition, the evolution laws of other hydration products are highly consistent with the analysis results of FTIR and SEM.

KEYWORDS

microstructure, sintered silt ash, hydration, thermodynamic modeling, portland cement

Introduction

Portland cement is used widely in buildings and structures due to its outstanding mechanical properties, reliability and low manufacturing cost relatively, which is one of the indispensable materials for human development at this stage. The production process of PC consumes a large amount of energy such as electricity and coal, and the mass ratio of carbon dioxide emitted to the cement produced is almost 1:1. In particular, the global cement industry emits 1.35 billion tons of greenhouse gas in recent year, accounting for 7% of total anthropogenic emissions (Xing et al., 2020), which increases the global warming significantly. In order to alleviate the above problems, people often use an appropriate proportion of fly ash (De la Varga et al., 2012; De la Varga et al., 2014; De la Varga et al., 2018),slag (Barati et al., 2011; Liu et al., 2019), metakaolin (Xing et al., 2018; Li et al., 2022) and other admixtures to replace part of the cement. While reducing carbon emissions, it also

improves the mechanical and durability properties of PC (Sujjavanich et al., 2017; Pelisser et al., 2018).

A large amount of waste silt produced by lakes, rivers, ocean dredging and urban sewage has threatened the ecological environment. It was estimated that China has produced 60 million tons of urban wet silt per recent year (Lin et al., 2022). The amount of waste silt produced by dredging of oceans and lakes is even greater, so it is very important to treat waste silt in a harmless manner (Chai et al., 2013; Wang et al., 2022). Silt contains various pollutants, and many countries prohibit opening marine environments to dispose of waste silt (Li et al., 2023). The silt produced in different environments has different components, but it is still clay minerals mainly such as illite (the main chemical composition is oxides such as silicon, aluminum, iron and calcium), animal and plant residues, and humus (mainly humic acid). Based on the fact that silt contains oxides such as Si, Ca, Al, Fe, adding silt to PC may improve its basic properties and some scholars have conducted research on this (Kappel et al., 2017). Since the untreated silt contains a large amount of free water and has poor fluidity, it is processed by drying, calcination and grinding (Chen et al., 2018; Chang et al., 2020) mainly. The treated silt is added to PC to replace part of the cement, reducing greenhouse gas emissions from the cement production process. Meanwhile, waste silt can also be consumed. Therefore, this approach has great significance for environmental protection and improvement of the performance of PC. Safi et al. (2011) replaced 10% and 20% of the weight of PC with calcined silt, and 30% of the weight of the PC with slag, and performed rheological and zeta potential tests on three samples to evaluate their electrokinetics and flow behavior. The results of the study indicated that the calcined silt was suitable as an additive to cement in the manufacture of self-compacting concrete. (Motisariya et al., 2023) replaced cement with different percentages of SSA (5, 10, 15, 20, 25), and evaluated the performance by setting time, rapid chlorine penetration test (RCPT) and XRD. The results showed that the compressive strength of 10% SSA mortar was higher than that of 20% SSA, and the addition of SSA benefited the cement. (Danish and Ozbakkaloglu, 2022) compared and analyzed the characteristics of SSA and the performance of SSA-modified cement-based composites, including hydration kinetics, mechanical properties, drying shrinkage, porosity and microstructural properties. This study found that 5%–10% SSA can be used to replace part of the cement, but the feasibility of large volumes of silt has not been studied. In the current research, it was mainly to study the properties of silt-modified cement by adding 5%–30% of silt into PC. Meanwhile, one of the purposes of silt-modified cement is to consume waste silt, so it is necessary to study adding a larger amount of silt to PC. In order to study the process of SSA-blended cement hydration, in addition to some basic experiments, numerical simulation should also be carried out to obtain more accurate information that is difficult to obtain in experiments (Ma et al., 2023).

This study conducted an in-depth study on the macroscopic properties and microscopic hydration products of SSA-blended cement. The resistance to chloride ion penetration was characterized by electric flux experiment. Fourier transform infrared spectroscopy (FTIR) was used to characterize the main hydration products. Meanwhile, the microscopic evolution of the hydration products was observed under the scanning electron microscopy (SEM), and the thermodynamic simulation of the hydration products was compared with the experimental results.

Materials and methods

Raw materials

The silt used in study was produced in Baiyangdian, Hebei. The cement used was P I 42.5 Portland cement produced in Fushun, Liaoning. The chemical composition of the silt and PC used was shown in Table 1. The silt had a high content of Si and Al. Its main components were SiO_2 and Al_2O_3, and it also contained a small amount of Fe_2O_3 and CaO. PC satisfied the requirements set out in GB 175-2020. The experimental water was ordinary tap water.

Treatment of dredged silt

Untreated silt was in a plastic state with high water content and low fluidity, so it could not be used in experiments directly. The treatment was divided into the following four steps. First, untreated silt was dried for 48 h using an electric blast drying oven which drying temperature was kept at 105°C; Second, the dried silt was ball-milled for 10 min with a ball-mill until it became powder; Third, the ball-milled silt powder was calcined at 800°C for 2 h continuously; Fourth, the high-temperature calcined silt was ball-milled again for 10 min until it was powdered. The reason for ball-milling again was that the silt calcined at high temperature was agglomerated. Figure 1.

Specimen preparation

In this study, the mass proportions of cement replaced by SSA were 0%, 10%, 30% and 50%, respectively. The water/cement was 0.35 uniformly. The mix ratio design of each group was shown in Table 2, among them, the first group was the reference group. According to GB/T 17671-2021, the mixed cement slurry was poured into the mold after the mixing and preparation were completed, and then vibrated 60 times to make it dense. The specimens were demoulded after 24 h forming and cured for 28 days under standard curing conditions.

Experiment methods

Mechanical property experiments

According to GB/T 17671-2021, EHC-300 automatic pressure testing machine was used to test the mechanical properties of the specimen. First, put the 40 mm*40 mm*160 mm prism on the flexural experiments bench of the testing machine, and kept the loading speed at 50N/s until it broke. After the bending experiment was completed, two half-sections were taken out for the compression experiment. During the loading process, a uniform loading rate of 2400N/s was maintained until the half-sections were broken. There were three samples for each mix ratio. The compressive strength and flexural strength were averaged.

TABLE 1 Chemical composition of raw materials (%).

Raw material	SiO_2	Al_2O_3	Fe_2O_3	CaO	MgO	SO_3	f-CaO	LOI
Cement	20.34	5.01	3.45	63.72	2.01	2.54	0.77	1.79
Silt	56.02	17.35	7.79	9.13	3.49	1.41	-	3.56

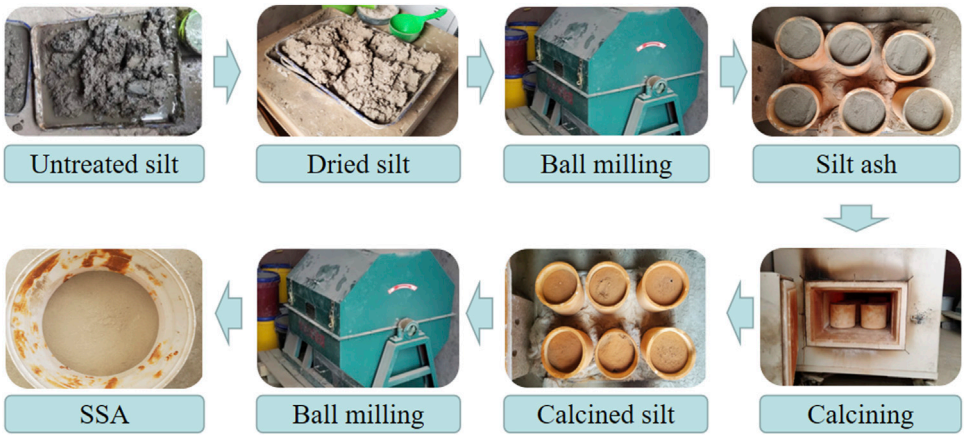

FIGURE 1
The treatment process of silt.

TABLE 2 Experiment mix ratio design.

	PC (%)	SSA (%)	Water (%)
SSA0	100	0	35
SSA10	90	10	35
SSA30	70	30	35
SSA50	50	50	35

TABLE 3 Classification of anti-chloride ion penetration performance (electric flux method).

Grade	High	Medium	Low	Lowest
Electric flux Q_S(C)	$Q_S \geq 4{,}000$	$2000 \leq Q_S < 4{,}000$	$1{,}000 \leq Q_S < 2000$	$100 \leq Q_S < 1{,}000$

Electric flux experiments

Corrosion resistance is important particularly when PC is used in harsh environment such as coastal area. The anti-chloride ion penetration performance of the specimen was tested by electric flux experiments. According to GB/T 50082-2009, firstly applied epoxy resin evenly on the side of the cylindrical specimen with a diameter of 100 mm and a height of 50 mm which were cured for 28 days, and then saturated it with a vacuum water saturator after the epoxy resin had cured. Subsequently, the chloride ion penetration experiment was carried out using the NEL-PEU concrete electric flux tester. Among them, the catholyte was 3% NaCl solution, and the anolyte was 0.3 mol/L NaOH solution. After turning on the power, recorded the initial current value I_0, and then recorded the current value every 10 min for 6 h. Table 3 shows the evaluation criteria for the electric flux data (Yang et al., 2021).

Fourier transform infrared spectroscopy

In view of the fact that different functional groups or chemical bonds have different absorption frequencies of infrared light, the distribution of hydration products in the sample can be judged by infrared light absorption spectrum. After the compressive experiment, took a small core sample from the broken test piece and then soaked it in isopropanol for 48 h. Dried it in a vacuum oven at 60°C for 48 h. The dehydrated samples were grounded into powder and their Fourier transform infrared spectra were obtained using a Thermo Scientific Nicolet iS20.

Scanning electron microscopy (SEM)

The scanning electron microscopy scans the surface of the sample by focusing a high-energy electron beam and excites various information, then collects, magnifies, and re-images the information to form the purpose of characterizing the microscopic morphology of the sample. Small core samples were taken from the broken test piece after the compressive strength experiment, and the hydration was stopped in the same manner as for the FTIR experiments described above. After spraying gold on the surface, specimens were placed under a scanning electron microscopy (FE-SEM, Apreo S LoVac, USA) to observe and record the microscopic morphology.

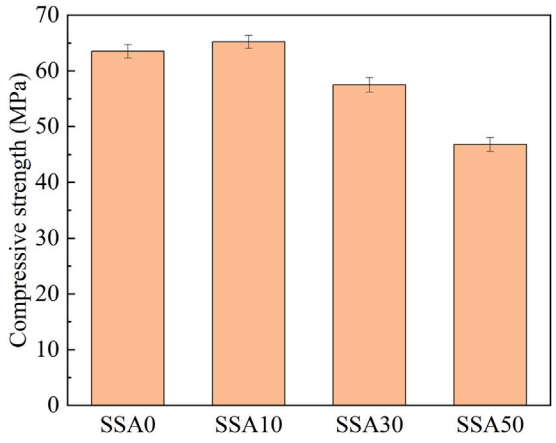

FIGURE 2
28-day compressive strength.

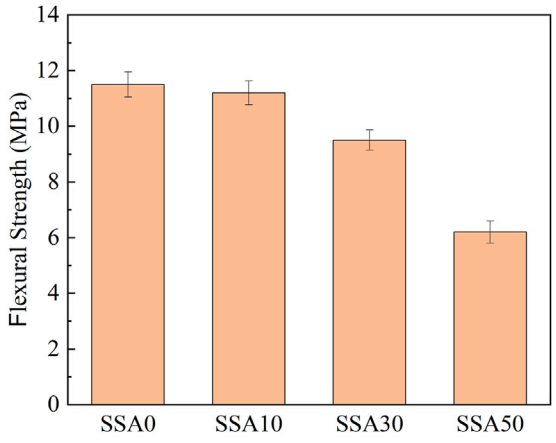

FIGURE 3
28-day flexural strength.

Thermodynamic simulation

Gibbs free energy is a thermodynamic function that can be used in chemical thermodynamics to judge the direction of a process.

$$\Delta G = \Delta H - T\Delta S$$

where, H, T, S, and G are state functions, ΔG represents the change of Gibbs free energy (J), ΔH represents enthalpy change (J), T represents temperature (°C), and ΔS represents entropy change (J/°C).

In view of this, in this study, thermodynamic calculations based on the Gibbs free energy principle were used to simulate the hydration product composition of cement at 28-day age under different contents of SSA. The above simulation relied on GEMS software, and all the thermodynamic parameters involved were taken from the Cemdate18 database (Lothenbach et al., 2019).

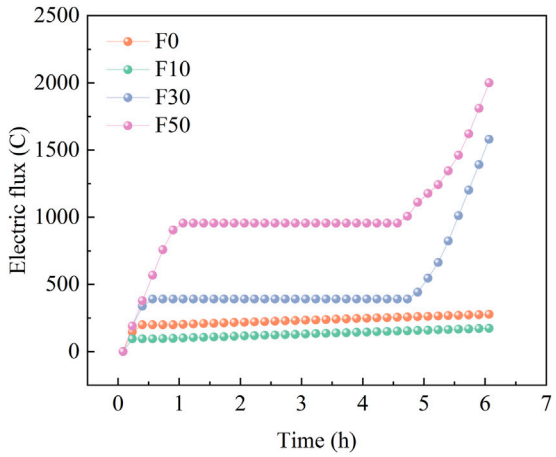

FIGURE 4
Electric flux curve.

Results and discussion

Mechanical properties

Compressive strength

Figure 2 shows the compressive strength of PC mixed with different SSA contents. It shows that the compressive strength increased first and then decreased with the increase of SSA. When the SSA content was 10%, the compressive strength was the largest and was 65.2 MPa, which was 2.6% higher than that of the reference group. On the one hand, this was due to the micro-filling effect. Low content of SSA filled the pores in the skeleton of cement hydration products and increased the nucleation sites of cement hydration products. On the other hand, it might be related to the pozzolanic activity of SSA. Considering that there was still a large amount of inert minerals in SSA, the hydration process of cement was delayed inevitably and the compressive strength decreased as the content of SSA continued to increase.

Flexural strength

Figure 3 shows the flexural strength of cement pastes mixed with different SSA contents. Different from the compressive strength, compared with the control group, the flexural strength showed a trend of gradually decreasing with the increase of SSA, suggesting that the addition of SSA had adverse effects on the development of the flexural strength of cement specimens. 10% SSA content reduced the flexural strength by 2.6%, 30% SSA content reduced the flexural strength by 10.7%, and when the content reached 50%, the flexural strength dropped by 47.8%. The flexural strength did not appear to increase in the compressive strength, which might be due to the low degree of SSA participation in hydration, resulting in an increase in the effective water/cement for cement hydration, resulting the hydration of the cement slurry under a small amount of SSA was accelerated significantly. Considering that the flexural strength tested the toughness of the specimen more and was more sensitive to micro-cracks, the increase in brittleness caused by

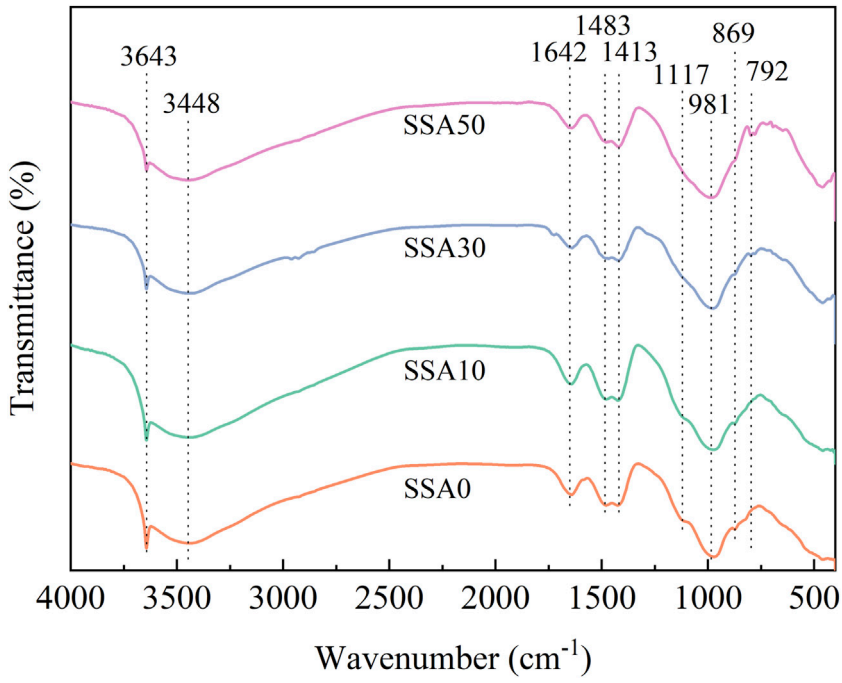

FIGURE 5
Infrared Spectrum.

accelerated hydration was not conducive to the improvement of the flexural strength.

Chloride ion penetration resistance

Figure 4 shows the curves of electric flux versus time for cement specimens with different SSA contents. Xiaoyan Li et al. (Li X. et al., 2022) showed in their research that the electric flux of the specimens affected mainly by porosity, pore size distribution and channel length. It can be observed from the experimental results that when the SSA contents were 0% and 10%, the curves grew extremely rapidly from 0 to 15 min, and then entered a gentle development stage. When the contents of SSA were 30% and 50%, the curves were in the rapid growth stage at 0–30 min and 0–1 h, and then entered the stable development stage. From the 5th hour, the two contents entered the stage of rapid growth again, which might be due to the relative instability of cement hydration products in the case of large SSA content. Moreover, the pores of the skeleton structure of the hydration product were filled with more unstable SSA, which may lead to the deterioration of the microstructure under the action of continuous current. In addition, the electric flux curve of 10% SSA remained at the lowest level among the four contents and was lower than the control group with 0% content, indicated that it could improve the chloride ion penetration resistance of cement specimens. In addition to the micro-filling effect, SSA underwent secondary hydration with $Ca(OH)_2$ generated from cement hydration, resulting in the quantity of C-S-H gels being replenished at a later stage. The cement gel led to the filling of the pore structure in the skeleton, which blocked the transmission channel of chloride ions to a certain extent, reducing the transmission rate of chloride ions, and thus improved the chloride ion penetration resistance of the cement specimen. At the 6th hour, the electric flux of 10% SSA still maintained the lowest level among the four mix ratios, and the electric flux of 0% SSA was 1.6 times that of 10% SSA. For 30% and 50% SSA, the electric flux was much higher than that of 10% SSA, which are 9.1 times and 11.5 times of 10% SSA respectively. According to the evaluation criteria in Table 3, the permeability grades of 0% SSA and 10% SSA were Lowest, while 30% and 50% SSA were Low and Medium respectively.

Hydration product

Figure 5 shows the FTIR spectra of different SSA contents. The band shown at 792 cm^{-1} was produced by Al-O bond vibrations. The proportion of Al_2O_3 in cement raw materials was low, but the proportion of Al_2O_3 in SSA was higher. There were more active Al_2O_3 in the silt calcined at high temperature, showed obvious peak positions at 30% and 50% SSA. The band near 869 cm^{-1} was likely to be caused by the asymmetric vibration of Al-O-H bond in $Al(OH)_6$ octahedral structure in ettringite. 0% and 10% contents produced a more obvious peak at this position, possibly generated by relatively more ettringite. It was observed that 981 cm^{-1} showed an obvious peak, which was generated by Si-O-Si vibration in C-S-H (Kapeluszna et al., 2021), by comparing the peak intensified here vertically under the four contents, it was found that the peak intensity became weaker gradually as the content of SSA increased. It was believed that the band at 1117cm^{-1} was caused by the asymmetric stretching vibration of the S-O bond in SO_4^{2-}, which was considered to be the fingerprint peak of Ettringite (Zhao

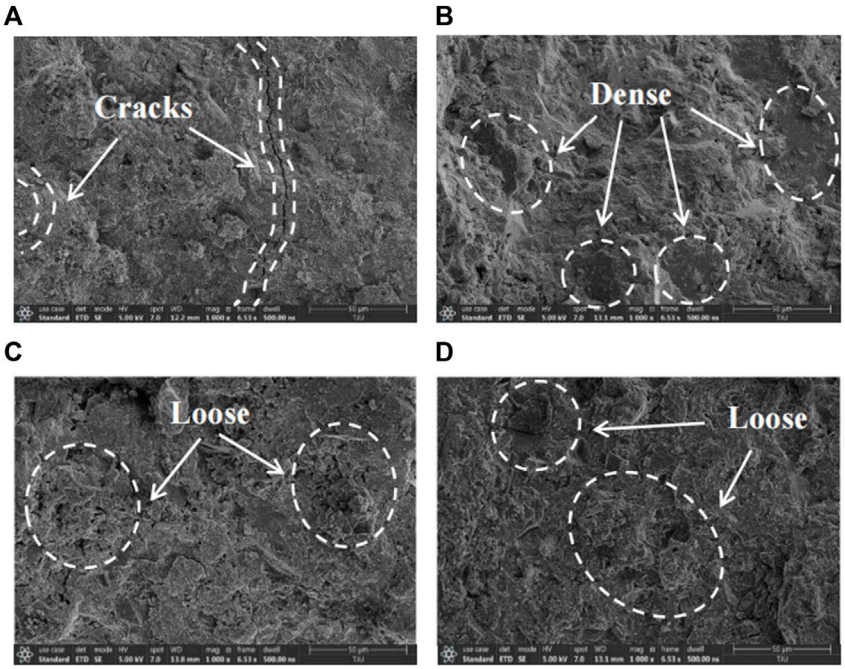

FIGURE 6
Micromorphology. **(A)** 0% SSA-28d, **(B)** 10% SSA-28d, **(C)** 30% SSA-28d, **(D)** 50% SSA-28d.

et al., 2023). The peak intensity here weakened gradually with the gradual increase of SSA content, indicated that the formation of ettringite decreased. The band at 1,413 cm^{-1} might be caused by the carbonization reaction during hardening, which was related to the stretching vibration of O-C-O. The peak here was more obvious for the spectrum of 50% content, which was guessed because the large content of SSA delayed the cement hydration process excessively, the formation of the skeleton structure of the hydration product was slower and the water consumption was slower, so it was easier to carbonization reaction occurs. The bands appeared around 1,642 cm^{-1} and 3,448 cm^{-1} were caused by the stretching and bending vibrations of the O-H bond of the structural water in the hydration product (Higl et al., 2021; Zhao et al., 2023). It could be seen that with the increase of SSA content, the peak intensity at 3,448 cm^{-1} decreased slightly, and the peak intensified at 1,642 cm^{-1} was the strongest at 10% content, indicated that the hydration products of the specimen with 10% SSA content were more and the hydration process was more sufficient. The band at 3,643 cm^{-1} was caused by the stretching vibration of the O–H bond in $Ca(OH)_2$ (Romano et al., 2019; Zhao et al., 2020), the peak intensified here weakened gradually with the increase of SSA content, which was caused by the increase of cement reduction rate and the consumption of $Ca(OH)_2$ by SSA.

Micromorphology

Figure 6 shows the micromorphology of the cement specimens at 1,000 magnifications for 28 days under different SSA contents. Compared with the other 3 mix ratios, the specimen with 10% SSA content was denser, which was inseparable from the pozzolanic reaction of amorphous SiO_2 and Al_2O_3 in SSA with less content to form calcium silicate hydrate. The secondary hydration of $Ca(OH)_2$ increased the amount of hydration products significantly. Meanwhile, the unreacted part of SSA might have a certain filling effect on the pores in the hydration product skeleton, making the structure more compact. Penetrating structural cracks were observed in the reference group, which might be shrinkage cracks caused by the increase of capillary pore pressure during the hydration process. It was observed that some loose unreacted SSA was attached to the surface of the specimens with 30% and 50% large amounts of SSA, and it could be guessed that there was an excess of unreacted SSA inside the specimen. An appropriate amount of SSA had a good filling effect on the skeleton of the hydration products, and excessive SSA might damage the compactness of the skeleton of the products, thereby affecting the macroscopic mechanical properties of the specimen.

Figure 7 shows the micromorphology of the specimens with different SSA contents under the scanning electron microscopy at 10000 magnifications. More ettringite and $Ca(OH)_2$ (Xu et al., 2022) were observed in the 0% content specimen. With the gradual increase of SSA content, the formation of ettringite in the specimen decreased gradually. But at 10% content, the formation of ettringite was maintained basically comparing with 0% of the specimen, and the development of ettringite was full slightly. $Ca(OH)_2$ was seldom observed in the 30% and 50% large-contents SSA specimens. On the one hand, the reason was that more $Ca(OH)_2$ was consumed by amorphous SiO_2 and Al_2O_3 in SSA. On the other hand, the reason was that more SSA were used instead of cement, resulting in a reduction of CaO in the mixture, which in turn resulted in a reduction in the generation of $Ca(OH)_2$. More C-S-H gels were observed in SSA10 specimens compared to

10.3389/fmats.2023.1264307

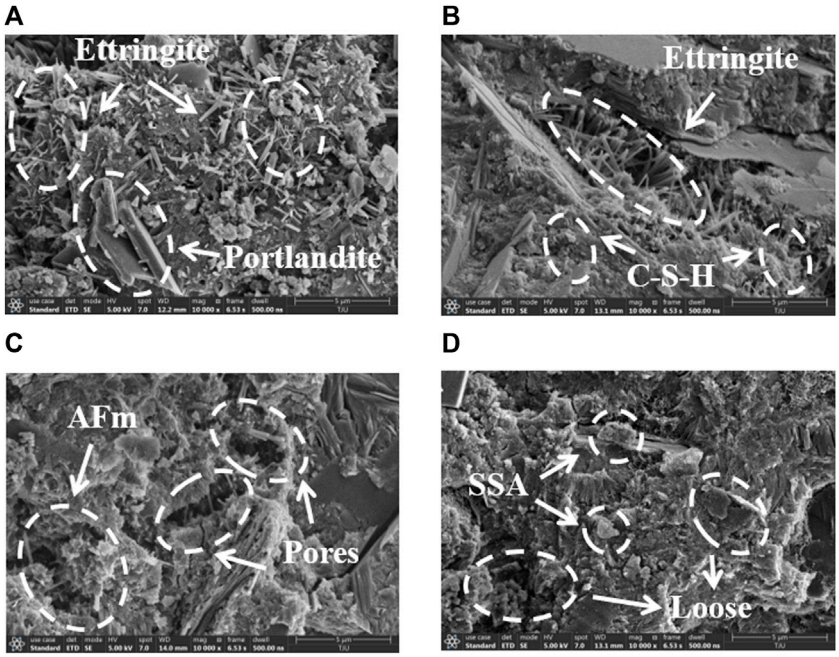

FIGURE 7
Distribution of hydration products. **(A)** 0% SSA-28d, **(B)** 10%SSA-28d, **(C)** 30%SSA-28d, **(D)** 50%SSA-28d.

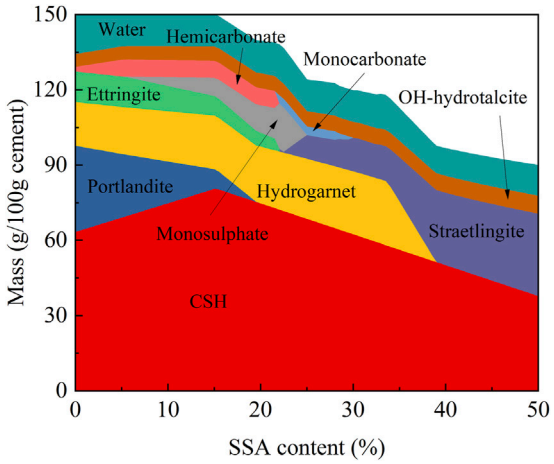

FIGURE 8
Thermodynamic simulation.

SSA0 specimens (Kim et al., 2021), while the C-S-H gel observed in the 30% and 50% contents decreased gradually, but the unreacted SSA increased gradually.

Thermodynamic simulation

Figure 8 shows the hydration product composition of different SSA contents incorporated into PC at reaction equilibrium simulated by thermodynamic method. With the process of cement hydration, the components of the mixture were consumed gradually and hydration products were formed. The main hydration products were C-S-H, Portlandite and Ettringite. The order of reaction rate in this process was alumina > alite > ferrite > belite (Zhang and Lv, 2023). The amount of C-S-H gel formation presented a trend of increased first and then decreased, reaching the maximum at about 15% SSA content. $Ca(OH)_2$ hardly existed when the SSA content was added more than 20%, which was consistent with the image shown in SEM, and also supported the conjecture of $Ca(OH)_2$ reduction in SEM. Hydrogarnet showed a decreasing trend gradually during the SSA content was from 0% to 40%, and almost no longer existed after 40% SSA content. OH-hydrotalcite existed in the content of 0%–50%SSA, but with the increase of the content, it showed a decreasing trend. When the content of Ettringite was 0%–22% in SSA, it tended to decrease gradually, which was also supported by FTIR and SEM. With the increase of SSA, Hemicarbonate was generated gradually, and then converted to Monocarbonate slowly (Bellmann et al., 2019; Georget et al., 2022). Noted that the results of the simulation did not maintain mass conservation, because the system only showed hydration products when simulating the hydration process, and as the SSA content increased, the part of the SSA in the mixture that did not participate in the reaction increasing gradually, and then the area of the blank part in the simulation experiments results was getting larger and larger, resulting in the non-conservation of the quality of the simulation results (He et al., 2023).

Conclusion

This study systematically explored the development of compressive strength, flexural strength and microstructure evolution of SSA-blended cement at 28 days of age by means of experiments and thermodynamic simulation. The conclusion of this paper is as follows:

1. Under different SSA contents, the compressive strength of cement at 10% was the highest, which was 2.6% higher than that at 0% SSA, but the flexural strength weakened with the increase of SSA content. Meanwhile, 10% SSA had the best resistance to chloride ion penetration, which was 37.3% higher than that of PC.
2. At 10% SSA content, the micro-filling effect and pozzolanic activity promoted the densification of the cement-based gelled framework, more hydration products, and a more complete hydration degree.
3. The results of thermodynamic simulation showed that the evolution of C-S-H, Portlandite and Ettringite were in good agreement with the results of SEM and FTIR microscopic experiments with the increase of SSA.

Data availability statement

The original contributions presented in the study are included in the article/supplementary material, further inquiries can be directed to the corresponding author.

Author contributions

ZPL: Investigation, Methodology, Writing–original draft. ZXL: Writing–review and editing, Validation. HZ: Data curation, Validation, Writing–original draft. QL: Resources, Software, Visualization, Writing–original draft. W-JL: Project administration, Supervision, Writing–original draft.

Funding

Financial support from the National Natural Science Foundation of China under the grant of U2006223 is gratefully acknowledged.

Conflict of interest

Author ZXL was employed by the company Poly Changda Engineering Co., Ltd.

The remaining authors declare that the research was conducted in the absence of any commercial or financial relationships that could be construed as a potential conflict of interest.

Publisher's note

All claims expressed in this article are solely those of the authors and do not necessarily represent those of their affiliated organizations, or those of the publisher, the editors and the reviewers. Any product that may be evaluated in this article, or claim that may be made by its manufacturer, is not guaranteed or endorsed by the publisher.

References

Barati, M., Esfahani, S., and Utigard, T. A. (2011). Energy recovery from high temperature slags. *Energy* 36 (9), 5440–5449. doi:10.1016/j.energy.2011.07.007

Bellmann, F., Majzlan, J., Grevel, K. D., Dachs, E., and Ludwig, H. M. (2019). Analysis of thermodynamic data of calcium aluminate monocarbonate hydrate. *Cem. Concr. Res.* 116, 89–94. doi:10.1016/j.cemconres.2018.10.012

Chai, Z. H., Yang, G. L., and Chen, M. (2013). Treating urban dredged silt with ethanol improves settling and solidification properties. *Korean J. Chem. Eng.* 30 (1), 105–110. doi:10.1007/s11814-012-0089-x

Chang, Z., Long, G., Zhou, J. L., and Ma, C. (2020). Valorization of sewage sludge in the fabrication of construction and building materials: A review. *Resour. Conservation Recycl.* 154, 104606. doi:10.1016/j.resconrec.2019.104606

Chen, Y., Wang, T., Zhou, M., Hou, H., Xue, Y., and Wang, H. (2018). Rice husk and sewage sludge co-combustion ash: leaching behavior analysis and cementitious property. *Constr. Build. Mater.* 163, 63–72. doi:10.1016/j.conbuildmat.2017.10.112

Danish, A., and Ozbakkaloglu, T. (2022). Greener cementitious composites incorporating sewage sludge ash as cement replacement: A review of progress, potentials, and future prospects. *J. Clean. Prod.* 371, 133364. doi:10.1016/j.jclepro.2022.133364

De la Varga, I., Castro, J., Bentz, D. P., Zunino, F., and Weiss, J. (2018). Evaluating the hydration of high volume fly ash mixtures using chemically inert fillers. *Constr. Build. Mater.* 161, 221–228. doi:10.1016/j.conbuildmat.2017.11.132

De la Varga, I., Castro, J., Bentz, D., and Weiss, J. (2012). Application of internal curing for mixtures containing high volumes of fly ash. *Cem. Concr. Compos.* 34 (9), 1001–1008. doi:10.1016/j.cemconcomp.2012.06.008

De la Varga, I., Spragg, R. P., Di Bella, C., Castro, J., Bentz, D. P., and Weiss, J. (2014). Fluid transport in high volume fly ash mixtures with and without internal curing. *Cem. Concr. Compos.* 45, 102–110. doi:10.1016/j.cemconcomp.2013.09.017

Georget, F., Lothenbach, B., Wilson, W., Zunino, F., and Scrivener, K. L. (2022). Stability of hemicarbonate under cement paste-like conditions. *Cem. Concr. Res.* 153, 106692. doi:10.1016/j.cemconres.2021.106692

He, J., Xiao, R., Nie, Q., Zhong, J., and Huang, B. (2023). High-volume coal gasification fly ash–cement systems: experimental and thermodynamic investigation. *Constr. Build. Mater.* 377, 131082. doi:10.1016/j.conbuildmat.2023.131082

Higl, J., Hinder, D., Rathgeber, C., Ramming, B., and Linden, M. (2021). Detailed *in situ* ATR-FTIR spectroscopy study of the early stages of C-S-H formation during hydration of monoclinic C3S. *Cem. Concr. Res.* 142, 106367. doi:10.1016/j.cemconres.2021.106367

Kapeluszna, E., Kotwica, L., and Nocun-Wczelik, W. (2021). Comparison of the effect of ground waste expanded perlite and silica fume on the hydration of cements with various tricalcium aluminate content - comprehensive analysis. *Constr. Build. Mater.* 303, 124434. doi:10.1016/j.conbuildmat.2021.124434

Kappel, A., Ottosen, L. M., and Kirkelund, G. M. (2017). Colour, compressive strength and workability of mortars with an iron rich sewage sludge ash. *Constr. Build. Mater.* 157, 1199–1205. doi:10.1016/j.conbuildmat.2017.09.157

Kim, H. S., Park, D. W., Oh, G. H., and Kim, H. S. (2021). Non-destructive evaluation of cement hydration with pulsed and continuous Terahertz electro-magnetic waves. *Opt. Lasers Eng.* 138, 106414. doi:10.1016/j.optlaseng.2020.106414

Li, W., Hua, L. M., Shi, Y. L., Wang, P. G., Liu, Z. C., Cui, D. B., et al. (2022a). Influence of metakaolin on the hydration and microstructure evolution of cement paste during the early stage. *Appl. Clay Sci.* 229, 106674. doi:10.1016/j.clay.2022.106674

Li, X. G., Wang, W. Z., Jian, S. W., Li, B. D., Gao, X., Huang, J. X., et al. (2023). Preparation of water storage ceramsite via dredged silt and biomass waste: pore formation, water purification and application. *Sci. Total Environ.* 859, 13. doi:10.1016/j.scitotenv.2022.160314

Li, X., Xu, F., Chen, B., Li, B., Chen, Z., Zhu, J., et al. (2022b). Investigation on the chloride ion erosion mechanism of cement mortar in coastal areas: from experiments to molecular dynamics simulation. *Constr. Build. Mater.* 350, 128810. doi:10.1016/j.conbuildmat.2022.128810

Lin, W., Liu, X., Ding, A., Ngo, H. H., Zhang, R. R., Nan, J., et al. (2022). Advanced oxidation processes (AOPs)-based sludge conditioning for enhanced sludge dewatering and micropollutants removal: A critical review. *J. Water Process Eng.* 45, 102468. doi:10.1016/j.jwpe.2021.102468

Liu, J. X., Yu, Q. B., Zuo, Z. L., Yang, F., Han, Z. C., and Qin, Q. (2019). Reactivity and performance of dry granulation blast furnace slag cement. *Cem. Concr. Compos.* 95, 19–24. doi:10.1016/j.cemconcomp.2018.10.008

Lothenbach, B., Kulik, D. A., Matschei, T., Balonis, M., Baquerizo, L., Dilnesa, B., et al. (2019). Cemdata18: A chemical thermodynamic database for hydrated portland

cements and alkali-activated materials. *Cem. Concr. Res.* 115, 472–506. doi:10.1016/j.cemconres.2018.04.018

Ma, H., Fan, H., Yu, H., and Peng, X. (2023). Effect of using grounded coral sand on hydration and strength development of portland cement paste: experimental and GEMS modelling investigation. *J. Build. Eng.* 68, 106001. doi:10.1016/j.jobe.2023.106001

Motisariya, K., Agrawal, G., Baria, M., Srivastava, V., and Dave, D. N. (2023). Experimental analysis of strength and durability properties of cement binders and mortars with addition of microfine sewage sludge ash (SSA) particles. *Mater. Today Proc.* 85, 24–28. doi:10.1016/j.matpr.2023.05.248

Pelisser, F., Vieira, A., and Bernardin, A. M. (2018). Efficient self-compacting concrete with low cement consumption. *J. Clean. Prod.* 175, 324–332. doi:10.1016/j.jclepro.2017.12.084

Romano, R. C. D., Bernardo, H. M., Maciel, M. H., Pileggi, R. G., and Cincotto, M. A. (2019). Using isothermal calorimetry, X-ray diffraction, thermogravimetry and FTIR to monitor the hydration reaction of Portland cements associated with red mud as a supplementary material. *J. Therm. Analysis Calorim.* 137 (6), 1877–1890. doi:10.1007/s10973-019-08095-x

Safi, B., Benmounah, A., and Saidi, M. (2011). Reología y potencial zeta de pastas de cemento con lodos de embalse calcinados y escorias granuladas de horno alto. *Mater. De. Construccion* 61 (303), 353–370. doi:10.3989/mc.2011.61110

Sujjavanich, S., Suwanvitaya, P., Chaysuwan, D., and Heness, G. (2017). Synergistic effect of metakaolin and fly ash on properties of concrete. *Constr. Build. Mater.* 155, 830–837. doi:10.1016/j.conbuildmat.2017.08.072

Wang, Y. K., Wang, G., Wan, Y. K., Yu, X., Zhao, J. C., and Shao, J. G. (2022). Recycling of dredged river silt reinforced by an eco-friendly technology as microbial induced calcium carbonate precipitation (MICP). *Soils Found.* 62 (6), 101216. doi:10.1016/j.sandf.2022.101216

Xing, H. F., Xiong, F., and Zhou, F. (2018). Improvement for the strength of salt-rich soft soil reinforced by cement. *Mar. Georesources Geotechnol.* 36 (1), 38–42. doi:10.1080/1064119x.2016.1278064

Xing, Z. Q., He, D. P., Wang, H. G., Ye, Z. F., and Yang, S. C. (2020). Study on soil mechanics and frost resistance of fly ash-metakaolin geopolymer. *Arabian J. Geosciences* 13 (18), 963. doi:10.1007/s12517-020-05954-y

Xu, Y. D., He, T. S., Ma, X. D., and Luo, R. Y. (2022). The influence of calcium sulphoaluminate cement on the hydration process of cement paste mixed with alkali free liquid accelerator. *Mater. Today Commun.* 33, 104622. doi:10.1016/j.mtcomm.2022.104622

Yang, J., Zeng, L., He, X., Su, Y., Li, Y., Tan, H., et al. (2021). Improving durability of heat-cured high volume fly ash cement mortar by wet-grinding activation. *Constr. Build. Mater.* 289, 123157. doi:10.1016/j.conbuildmat.2021.123157

Zhang, J. T., and Lv, T. (2023). Hydration and durability of low-heat cementitious composites for dam concrete: thermodynamic modeling and experiments. *Front. Mater.* 10, 9. doi:10.3389/fmats.2023.1120520

Zhao, Q., Tu, J. W., Han, W. W., Wang, X., and Chen, Y. Z. (2020). Hydration properties of portland cement paste with boron gangue. *Adv. Mater. Sci. Eng.* 2020, 1–9. doi:10.1155/2020/7194654

Zhao, Q. X., Lv, T., Liang, H., Zhang, J. T., and Zhang, J. R. (2023). Enhancement of sintered sludge ash-modified cement paste with CaSO4 and CaCl2. *Constr. Build. Mater.* 383, 131245. doi:10.1016/j.conbuildmat.2023.131245